processes

MDPI

Article

Simultaneous Achievement of High-Yield Hydrogen and High-Performance Microwave Absorption Materials from Microwave Catalytic Deconstruction of Plastic Waste

Hui Wang [1], Bowen Zhang [1], Pan Luo [1], Kama Huang [1,2] and Yanping Zhou [1,2,*]

[1] College of Electronics and Information Engineering, Sichuan University, Chengdu 610065, China; wanghui2@stu.scu.edu.cn (H.W.); zhangbowen2@stu.scu.edu.cn (B.Z.); luopan@stu.scu.edu.cn (P.L.); kmhuang@scu.edu.cn (K.H.)

[2] State Key Laboratory of Polymer Materials Engineering, Sichuan University, Chengdu 610065, China

* Correspondence: ypzhou11@scu.edu.cn

Abstract: Here, $FeAlO_x$ catalytic deconstruction of polyethylene in a domestic microwave oven is reported. With the starting weight ratio of $FeAlO_x$ to polyethylene at 1:1, the concentration and yield of H_2 reach up to 67.85 vol% and 48.1 mmol $g^{-1}{}_{plastic}$, respectively. CNTs@Fe_3O_4/Fe_3C/Fe composite, which exhibits excellent microwave absorption properties, is generated simultaneously. The minimum reflection loss (RL_{min}) of the solid product reaches −54.78 dB at 15 GHz with an effective absorption bandwidth of 4.5 GHz at the thickness of 1.57 mm.

Keywords: catalytic cracking; plastic waste; carbon nanotubes; hydrogen; microwave absorption

check for updates

Citation: Wang, H.; Zhang, B.; Luo, P.; Huang, K.; Zhou, Y. Simultaneous Achievement of High-Yield Hydrogen and High-Performance Microwave Absorption Materials from Microwave Catalytic Deconstruction of Plastic Waste. *Processes* **2022**, *10*, 782. https://doi.org/10.3390/pr10040782

Academic Editor: María José Martín de Vidales

Received: 16 February 2022
Accepted: 13 April 2022
Published: 16 April 2022

1. Introduction

According to an estimate, the total amount of plastic waste in landfills or the natural environment will reach 12 billion tons by 2050 [1]. Thus, plastic waste recovery technologies are warmly welcomed to reduce the negative impact of plastics, such as biological recycling, physical recycling, and thermochemical recycling technology [2]. Among them, thermochemical recycling technologies, such as pyrolysis and gasification, have been widely studied for fuel production [3,4]. In particular, catalytic cracking is an effective plastic recycling technology to produce high-value hydrogen [5–7]. For example, Yao et al. [7] obtained an H_2 concentration and H_2 yield up to 73.93 vol% and 42.36 mmol $g^{-1}{}_{plastic}$, respectively, from catalytic conversion of plastic waste using a Ni-Fe bimetallic catalyst. Zhang et al. [8] produced H_2-rich syngas from biomass and plastic waste with a Ni-Fe@Nanofibers/Porous carbon catalyst. The corresponding total gas and hydrogen yields were 63.17 and 24.73 mmol g^{-1}, respectively. Undoubtedly, converting plastic waste into clean fuel is an attractive way to alleviate the environmental pollution and energy crisis. Nevertheless, the application of the residual carbon-containing solid is yet to be explored.

With the rapid development of information, the application of electronic devices, radar, military aircraft, and satellite communications has increased greatly, along with serious electromagnetic pollution and interference [9,10]. Thus, the preparation of lightweight, low cost, and efficient microwave absorption (MA) materials has received considerable interest [11–13]. Among them, carbon-based materials are widely concerned because of their advantages of light weight, good electrical conductivity, and adjustable dielectric loss [14–16]. Particularly, pores could contribute to the multiple reflection and diffraction of the microwave. Therefore, porous carbon structures in the form of fibers, tubes, or spheres have been extensively investigated to achieve high MA performance [16–18]. Compositing carbon with magnetic particles is an effective method to enhance the attenuation of microwave energy due to the introduction of magnetic loss capacity and the improvement of impedance matching. For example, Zhao et al. [19] prepared a Co@crystalline carbon@carbon aerogel composite with a yolk-shell structure at 900 °C, exhibiting a maximum

reflection loss (RL_{max}) of −43 dB at the thickness of 1.5 mm at 17.9 GHz. Qiu et al. [20] synthesized a nickel/carbon nanotubes composite (Ni/CN) via in-situ pyrolysis of Ni MOF at 700 °C, showing an RL_{max} of −65 dB with a low filler loading of 10 wt% and a thickness of 1.9 mm.

In this work, we proposed a microwave-assisted catalytic strategy to achieve high-yield hydrogen and high-performance microwave absorption materials from the catalytic deconstruction of polyethylene (PE) simultaneously. Iron aluminum oxide ($FeAlO_x$) was used as the catalyst. The deconstruction reaction was initiated by a small piece of carbon fiber cloth (CFC), which has strong microwave absorption properties. The concentration and yield of H_2 reached up to 67.85 vol% and 48.1 mmol $g^{-1}{}_{plastic}$, respectively, with the starting weight ratio of $FeAlO_x$ to PE at 1:1. Moreover, the RL_{min} of the solid product reached −54.78 dB at 15 GHz with an effective absorption bandwidth (EAB) of 4.5 GHz at the thickness of 1.57 mm.

2. Materials and Methods

2.1. Material

Iron nitrate (Fe $(NO_3)_3 \cdot 9H_2O$, analytical grade), aluminum nitrate (Al $(NO_3)_3 \cdot 9H_2O$, analytical grade), and citric acid were purchased from Shanghai Aladdin Chemical Corporation. Carbon fiber cloth (CFC) was purchased from Jingzhou HOT-Material Co., LTD. The raw material comes from pulverized plastic waste (300 mesh). Standard concentrations (1%) of CO, CO_2, and the mixtures of CH_4, C_2H_6, C_2H_4, C_3H_8, and C_3H_6 were purchased from the China National Institute of Testing technology. Pure H_2 (100%) was obtained by a hydrogen generator (CHE-300, CEAULIOHT Co., LTD., Beijing, China).

2.2. Synthesis Method

2.2.1. Preparation of FeAlOx Catalyst

$FeAlO_x$ catalyst was prepared with reference to the study by Jie et al. [21]. In detail, an appropriate amount of Fe $(NO_3)_3 \cdot 9H_2O$, Al $(NO_3)_3 \cdot 9H_2O$, and citric acid were mixed with a molar ratio of Fe to Al to citric acid of 1:1:1, which was stirred continuously on a heating table at 120 °C until a viscous orange gel formed. Then, the gel was dried at 90 °C overnight. Next, the powder was calcined in air at 350 °C for 3 h with a heating ratio of 10 °C min^{-1}. Finally, the catalyst was ground into fine particles.

2.2.2. Microwave-Assistant Catalytic Deconstruction of PE

First, different weight ratios of the $FeAlO_x$ catalyst (0.2, 0.4, and 0.8 g) and PE powder (0.4 g) were physically mixed and transferred into a custom-made quartz tube. Then, a piece of CFC (1 × 4 cm) was embedded in the mixtures vertically. Before irradiation, high purity N_2 (99.99%) was purged for 10 min to expel the air completely. Next, the quartz container was placed in a commercial microwave oven (Galanz, G90F23CN3PV-BM1, Foshan, China) and irradiated at the power of 900 W for 6 min. The reaction systems with different $FeAlO_x$ weights were labeled as Catalyst/PE−0.5, Catalyst/PE−1, and Catalyst/PE−2, respectively.

2.3. Measurement of Gaseous Products

The gas volume fraction (C) was measured by a Gas Chromatograph (GC-7920, CEAULIOHT Co., LTD., Beijing, China, China) equipped with a thermal conductivity detector (TCD) and Flame ionization detector (FID). The operating temperature was 200 °C. H_2 was detected by TCD equipped with a TDX-01 column (3 m × 3 mm, C.N. YJ0441). CO and CO_2 were detected by FID equipped with a TDX-01 column (1.5 m × 3 mm, C.N. YJ6027), and the mixtures of CH_4, C_2H_6, C_2H_4, C_3H_8, and C_3H_6 were detected by FID equipped with an XP- Al_2O_3/NA2S04 column (50 m × 0.53 mm i.d., 20.0 μm film thickness,

C.N. 23505200). N_2 was used as a carrier gas in the analysis. The molar yield of gas product (mmol g^{-1}) was defined as:

$$Y = \frac{C \cdot V}{V_m \cdot M}, \quad (1)$$

where C (%) represents the volume concentration; V (mL) means the total volume of gaseous products; V_m (mol/L) represents the molar volume with a value of 23.3 at standard atmospheric pressure (101 kPa) and 10 °C (laboratory temperature). M is the mass of PE with the value of 0.4 g.

2.4. Characterization

The crystalline structure of the solid product was recorded on X-ray diffractometry (XRD, DX-2700, Dandong Haoyuan Instrument Co., LTD., Dandong, China) using Cu Kα radiation at 40 kV and 30 mA, and the scanning range (in 2θ) was 5° to 90°. The microstructure was analyzed by Field emission scanning electron microscope (FESEM, AZtec X-Max 50, Oxford, UK). The hydrogen and hydrocarbons (C1–C5) of gaseous products were determined via a Gas Chromatograph (GC-7920, CEAULIOHT Co., LTD., Beijing, China) equipped with TCD and FID detectors. The relative complex permittivity and permeability of solid product were measured on an Agilent E8363C vector network analyzer (E8363C, Agilent Technologies, Inc., Palo Alto, Santa Clara, CA, USA) equipped with a coaxial fixture (Φ out = 7.00 mm, Φ in = 3.04 mm) in the frequency range of 2.0–18.0 GHz.

3. Results and Discussion

CFC acts as a microwave susceptor to trigger the catalytic cracking reaction. After the reaction, CFC can be easily taken out and separated from the residual carbon and catalyst particles. The concentrations and yields of gaseous products are shown in Figure 1. Since the concentrations of hydrocarbons, such as C_2H_6, C_3H_6, and C_3H_8, are extremely low, these gases fractions are combined into the category of "others" to simplify the analysis. For the Catalyst/PE−0.5 system, it can be seen that the gaseous products are dominated by H_2 (40.5 vol%), followed by C_2H_4 (23.5 vol%), CH_4 (18.2 vol%), CO (7.0 vol%), and CO_2 (1.6 vol%). Their corresponding yields are 16.7, 9.7, 7.6, 2.8, and 0.6 mmol $g^{-1}{}_{plastic}$, respectively (Figure 1a,b). The concentration and yield of H_2 are up to 67.8 vol% and 48.1 mmol $g^{-1}{}_{plastic}$, respectively, in the Catalyst/PE−1 system (Figure 1c,d). The yield of CO increases to 14.4 mmol $g^{-1}{}_{plastic}$ while the yield of C_2H_4 and CH_4 drops to 3.63 and 4 mmol $g^{-1}{}_{plastic}$. The concentration and yield of H_2 are 59.6 vol% and 46.5 mmol g^{-1}, respectively, for the Catalyst/PE−2 system (Figure 1e,f), where the yield of CO is up to 26.5 mmol g^{-1}. Based on the above, it can be concluded that the weight ratio of catalyst/PE exhibits a great influence on the gaseous product compositions and H_2 yields. The weight ratio at 1:1 is proved to be the most effective. Too much catalyst does not help achieve higher hydrogen yields but rather promotes the production of CO. The H_2 yield and concentration with different metal-based catalysts between our results and the reported literatures are compared in Table 1, which shows $FeAlO_x$ catalyst owned excellent catalytic activity [7,22–24].

About the catalytic mechanism, here we propose that they mainly include three stages. Firstly, carbon fiber cloth generates a large amount of heat under the action of microwaves, which is rapidly transferred to the plastic and catalyst particles, causing the plastic to be melted and the catalyst to be activated. Secondly, at the active site of the iron catalyst, the C-H bonds of the plastic polymer break off, thus H_2 and intermediate compounds such as alkenes/aromatics are produced. Thirdly, the intermediate compounds produce H_2 further under heating. With the enriched heating rate due to the special microwave irradiation, the first and second steps are usually present at the same time, resulting in high H_2 yields.

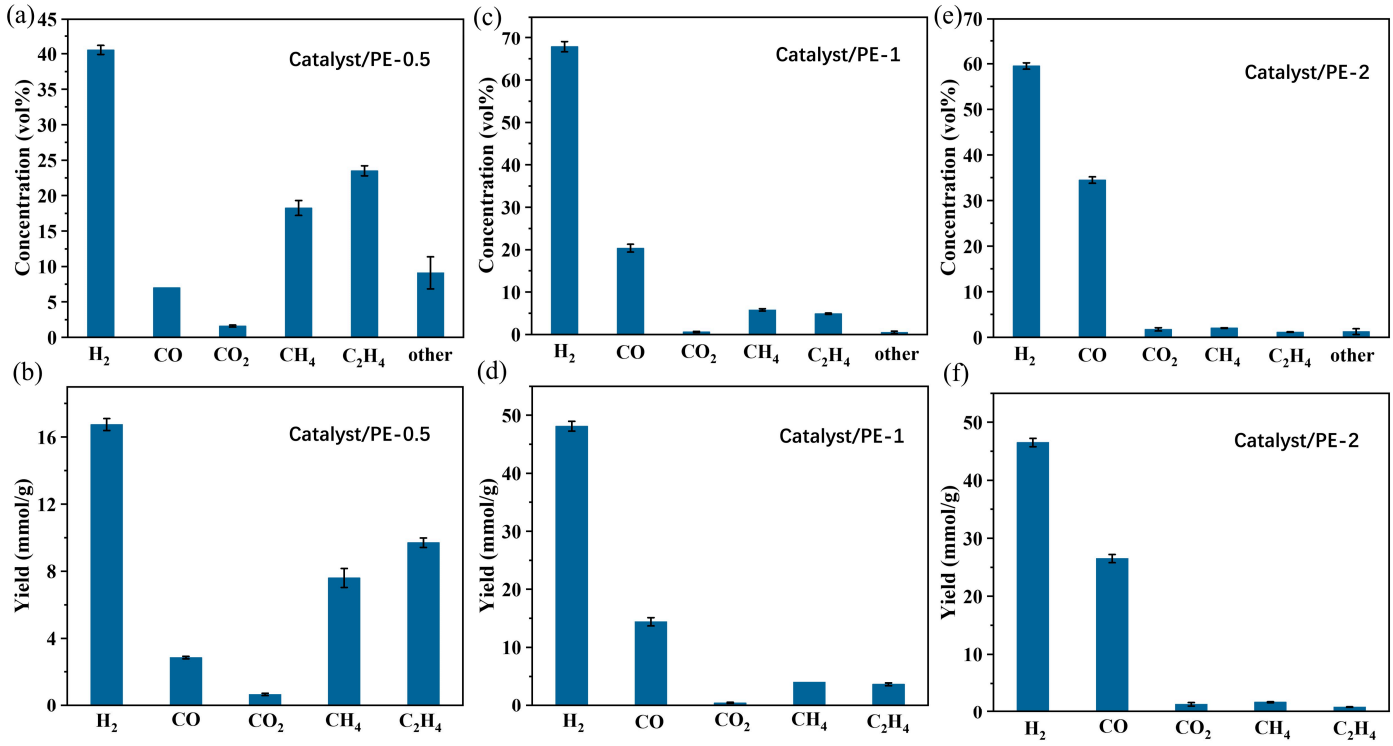

Figure 1. (**a**,**c**,**e**) The concentrations and (**b**,**d**,**f**) yields of H_2 in different reaction systems.

Table 1. Comparison of the H_2 yield and concentration with different catalysts between our results and those reported in the literature.

Material	Method	Catalyst	H_2 Concentration (vol%)	H_2 Yield (mmol/g)	Ref.
Mixed plastics	Conventional catalyst pyrolysis	$NiFe31/Al_2O_3$	69.98	36.2	[7]
High density polyethylene (HDPE)/polyvinyl chloride (PVC)	Catalyst pyrolysis and steam reform	Ni-Mn-Al	72.3	42.8	[22]
Low density polyethylene (LDPE)	Conventional catalyst pyrolysis	Fe/Al_2O_3	51.0	19.5	[23]
Polypropylene (PP)/polyethylene (PE)	Pyrolysis–gasification	$H\text{-}Ni/Al_2O_3$	36.85	32.4	[24]
Polyethylene (PE)	Microwave catalyst pyrolysis	$FeAlO_x$	67.85	48.1	This work

Hence, the solid residual from the Catalyst/PE−1 system was characterized, and its microwave absorption performance was examined. The XRD spectra are shown in Figure 2a. As can be seen, peaks located at 30.06°, 35.41°, 43.03°, 56.91°, and 62.49° correspond to the Fe_3O_4 phase (JCPDS card No. 76-1849), peaks located at 37.63°, 42.88°, 43.76°, 44.55°, 44.97°, 45.88°, 48.57°, and 49.11° correspond to Fe_3C (PDF-72-1110, and peaks for iron at 44.67° and 65° are observed [25]. Besides, the appearance of a peak around 26° suggests graphitized carbon formed under microwave irradiation. Figure 2b,c shows the product's SEM images. A large number of uniform CNTs with a tube diameter of about 50 nm can be clearly seen. The formation of carbon nanotubes is probably attributed to the catalyzing effect of the iron particles [26,27] and is regarded as very beneficial for the microwave absorption performance. Carbon nanotubes contribute to forming a 3D continuous conductive network, which provides high-speed transmission channels for charge motion and thus increases the conductive loss [28]. In addition, the abundant tubular structure helps to provide more boundaries, which makes the interface polarization effect enhanced [29].

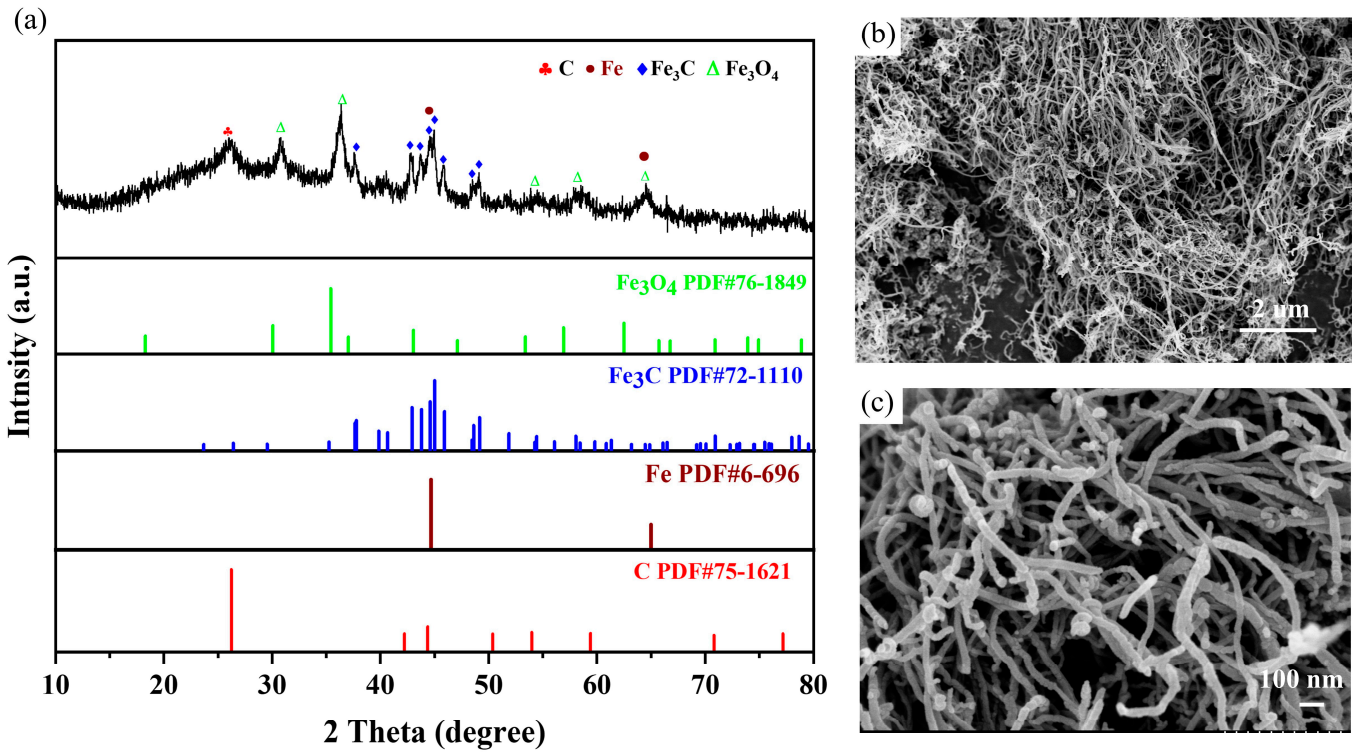

Figure 2. (**a**) The XRD spectra and (**b**,**c**) FESEM images of the solid residual from the Catalyst/PE−1 system.

Reflection loss (*RL*) is an intuitive parameter to evaluate the MA performance of a material. According to the transmission line theory, the *RL* with thickness and frequency can be calculated as follows:

$$RL(dB) = 20\log\left(\left|\frac{Z_{in} - Z_0}{Z_{in} + Z_0}\right|\right), \quad (2)$$

$$Z_{in} = Z_0\sqrt{\frac{\mu_r}{\varepsilon_r}}tanh\left[j\left(\frac{2\pi fd}{c}\right)\sqrt{\mu_r\varepsilon_r}\right], \quad (3)$$

Here, Z_{in} is the input impedance of the absorber and Z_0 is the impedance of materials in free space, f is the frequency of the electromagnetic wave, d is the layer thickness of the sample, c stands for the speed of light in vacuum, ε_r (ε'-$j\varepsilon''$) and μ_r (μ'-$j\mu''$) correspond to the relative complex permittivity and permeability, respectively. Figure 3a,b shows the three-dimensional (3D) and 2D *RL* value of the solid residue from the Catalyst/PE−1 system in the frequency range of 2–18 GHz at a loading of 30 wt%. As can be seen, the solid residual exhibits excellent MA performance in the Ku band with a low thickness. In detail, the minimum reflection loss ($RL_{\min}$) of the product is −54.78 dB at 15 GHz with an EAB of 4.5 GHz (12.9–17.4 GHz) at the thickness of 1.57 mm. Meanwhile, the sample has an acceptable MA performance in other frequency ranges, delivering an $RL_{\min}$ value of −26.6 dB at 9.2 GHz with an EAB of 2.84 GHz (8–10.84 GHz) at the thickness of 2.4 mm in X-band and an $RL_{\min}$ value of −18.45 dB at 7 GHz with an EAB of 2.04 GHz at a thickness of 3.17 mm in C-band. Compared with the microwave absorption performance of various carbon-nanotube-based magnetic composites in previous reports shown in Table 2 [30–34], the solid residue of the catalyst/PE−1 system is a competitive candidate for an ideal absorber material in terms of absorption intensity, effective absorption bandwidth, and thickness.

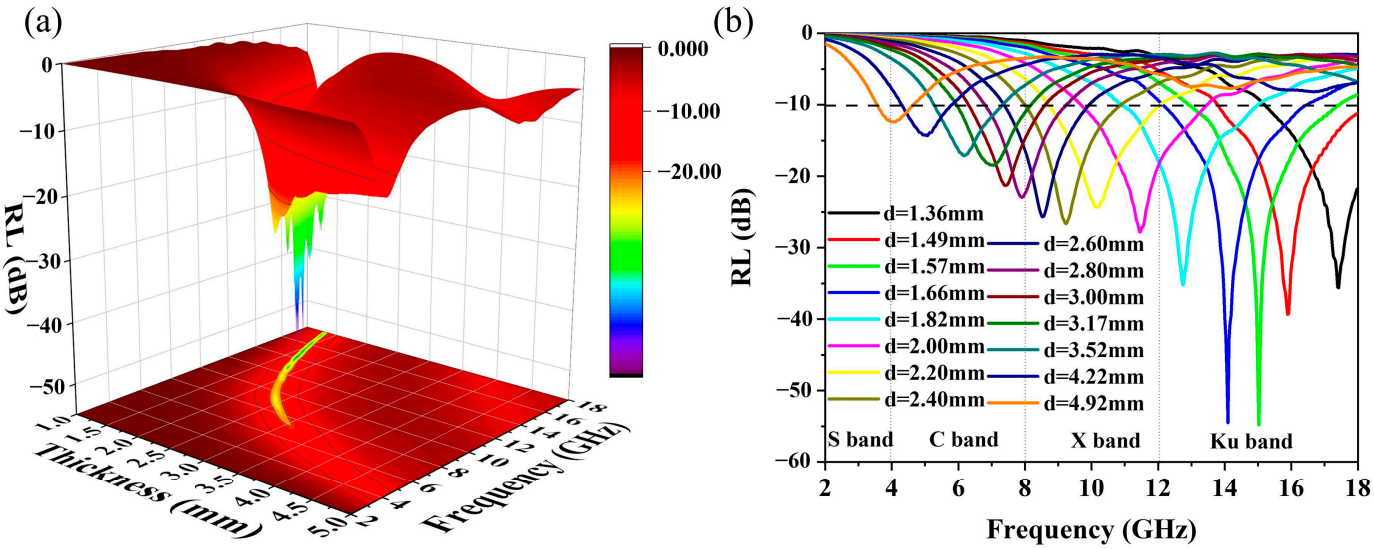

Figure 3. The 3D (**a**) and 2D (**b**) representation of *RL* values of the solid residue from the Catalyst/PE−1 system.

Table 2. Microwave absorption performances of various carbon-nanotube-based magnetic composites in previous reports compared with CNTs@Fe_3O_4/Fe_3C/Fe composite.

Sample	Weight (wt%)	Thickness (mm)	RL_{min} (dB)	Effective Bandwidth/Frequency (GHz)	Ref
Fe_3O_4/CNT/poly	100	/	−53.3	8.1 (/)	[25]
PANI/Fe_3O_4/CNT	20	4.0	−16	7.0 (8–15)	[26]
rGO/CNT@Fe_3O_4	30	2	−28.57	3 (9.7–12.7)	[27]
Fe_3O_4/CNT	50	4.4	−51.3	3.9 (/)	[28]
Fe_3O_4/CNT	/	5.5	−36.72	~6.5 (4–6.5,14–18)	[29]
CNT@Fe_3O_4/Fe_3C/Fe	30	1.57	−54.78	4.5 (12.9–17.4)	This work

In order to better understand the MA mechanism of the solid product from the Catalyst/PE−1 system, its electromagnetic parameters are interpreted further and displayed in Figure 4. The real parts of the relative complex permittivity (ε') and permeability (μ') characterize the ability of the material to store electrical and magnetic energy, and the imaginary parts (ε'' and μ'') represent the ability to dissipate electrical and magnetic energy, respectively [35]. The real parts (ε') and imaginary parts (ε'') of the relative complex permittivity of the sample are in the range of 9.5–16.0 and 2.5–9.5 in the frequency of 2–18 GHz, respectively (Figure 4a,b). The values of ε' and ε'' decrease with the increase in frequency, which is ascribed to the increased polarization hysteresis vs. the higher frequency electric field variation [36–41]. Furthermore, the several distinct peaks in the curves of ε'' can be explained by the polarization relaxation [41–44]. The dielectric tangent loss factor $\tan\delta_e$ ($\varepsilon''/\varepsilon'$) represents the dielectric loss capability. Increasing the $\tan\delta_e$ value of a material is helpful to improve its dielectric loss performance. The trend of $\tan\delta_e$ is consistent with ε'', with values fluctuating between 0.25 and 0.6 (Figure 4c). For pure carbon materials, the real parts (μ') and imaginary parts (μ'') of the relative complex permeability are generally considered to be 1 and 0, respectively, on account of the non-magnetic property. The values of μ' and μ'' of the solid product from the Catalyst/PE−1 system are in the range of 1.0–1.2 and 0.0–0.16, respectively, over the frequency of 2–18 GHz (Figure 4d,e) because of the existence of Fe_3O_4 and Fe, as indicated by XRD spectra. The magnetic loss tangent $\tan\delta_m$ (μ''/μ') could be used to help analyze the magnetic loss capacity. The trend of the $\tan\delta_m$ curve is consistent with μ'' with a value range of 0.0–0.16 at 2–18 GHz (Figure 4f). Therefore, the excellent MA performance of the sample is attributed to the synergistic effect of dielectric loss and magnetic loss. The value of the dielectric loss tangent is higher than

that of the magnetic loss tangent, which indicates that the loss of the material is dominated by the dielectric loss.

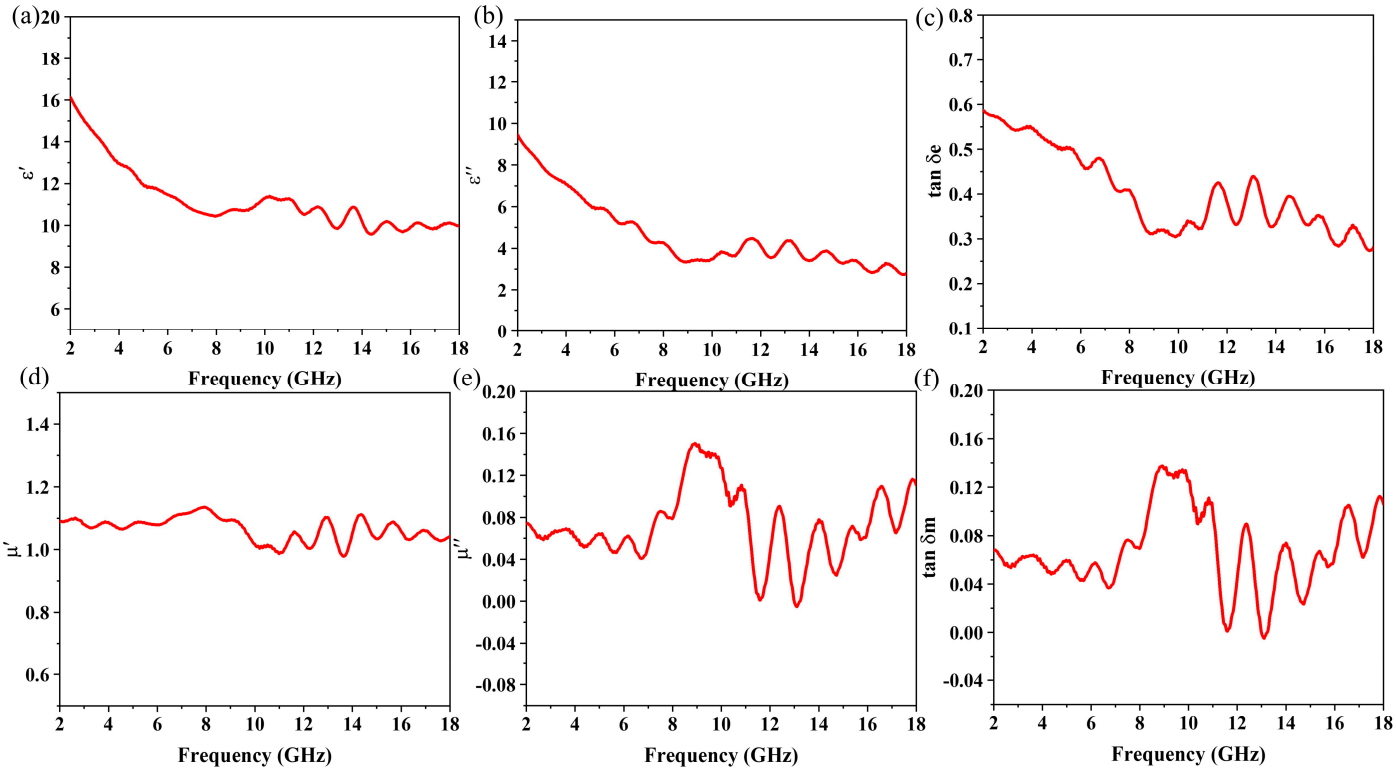

Figure 4. Electromagnetic parameters of the solid residue from the Catalyst/PE−1 system: (**a**) ε′, (**b**) ε″, (**c**) dielectric loss (tan δe), (**d**) μ′, (**e**) μ″, and (**f**) magnetic loss (tanδm).

It is well known that impedance matching and attenuation properties are the key factors that must be considered when analyzing the MA performance of a material. The normalized characteristic impedance ($Z = |Z_{in}/Z_0|$) can be calculated by Equation (3) [42], and the attenuation constant (α) is based on the following equation [45,46]:

$$\alpha = \frac{\sqrt{2}\pi f}{c}\sqrt{(\mu''\varepsilon'' - \mu'\varepsilon') + \sqrt{(\mu''\varepsilon'' - \mu'\varepsilon')^2 + (\mu'\varepsilon'' + \mu''\varepsilon')^2}}, \quad (4)$$

Impedance matching ratio Z reflects the ability of electromagnetic waves to enter the microwave absorber. The value of Z closes to 1 indicates that the absorbing material has better impedance matching. Figure 5a shows the sample's impedance matching with thickness of 1.57 mm. It is obvious that the sample matches better in 12–18 GHz band than 2–12 GHz band. In particular, the value of Z fluctuates around 1 in the frequency range of 12–16 GHz, so most of the electromagnetic waves enter into the material. Since the Z value is far below 1 in the frequency of 2–8 GHz, most of the electromagnetic waves are reflected at the surface of the absorber. The value of the attenuation constant increases from 55 to 234 as the frequency increases from 2 to 18 GHz (Figure 5b), which is much higher than previously reported for pure carbon (below 25) [47]. The above analysis shows that the excellent MA performance of the solid residue of the Catalyst/PE−1 system is due to the good impedance matching and high attenuation constants, especially in the frequency range of 14–18 GHz.

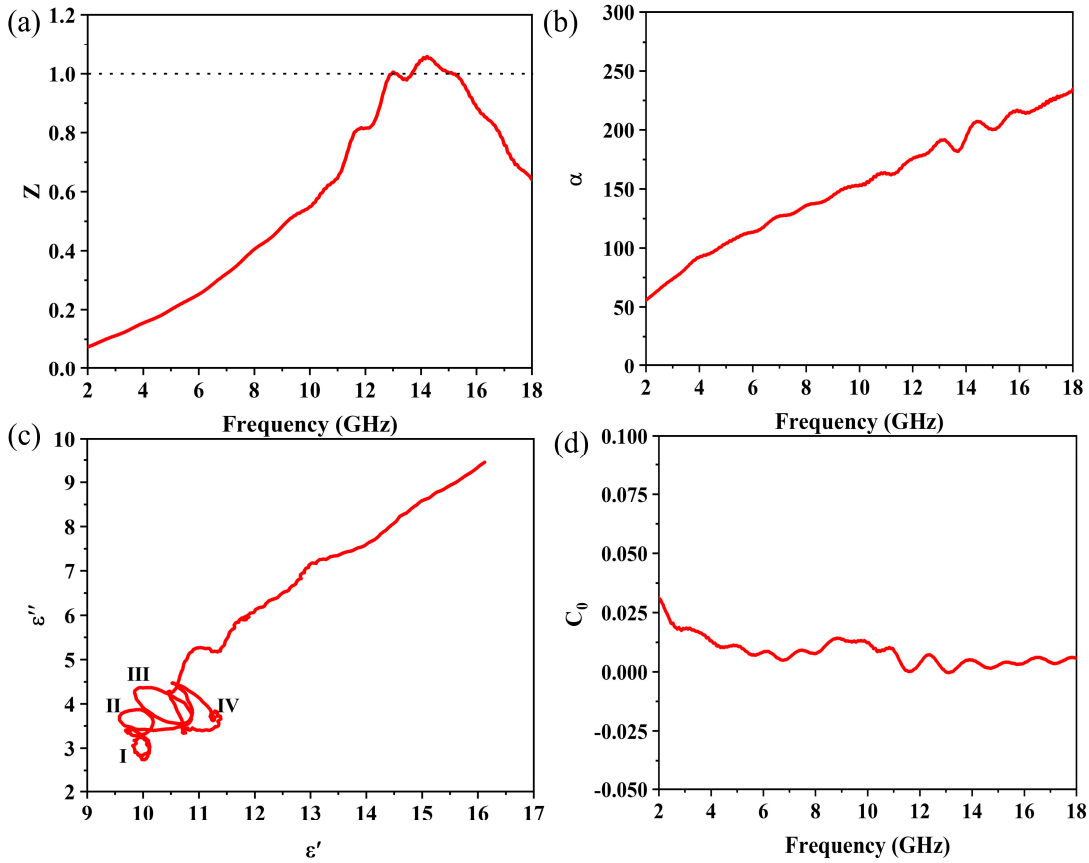

Figure 5. Electromagnetic parameters of the solid residue of the Catalyst/PE−1 system: (**a**) impedance matching ratio (*Z*), (**b**) attenuation constant (**a**), (**c**) typical Cole–Cole semicircles, and (**d**) C_0 curve.

Debye-relaxation is a common method used to analyze the polarization mechanism, which is usually defined by the following equation [48]:

$$\left(\varepsilon' - \frac{\varepsilon_s + \varepsilon_\infty}{2}\right)^2 + \left(\varepsilon''\right)^2 = \left(\frac{\varepsilon_s - \varepsilon_\infty}{2}\right)^2, \tag{5}$$

Here, ε_s means the static permittivity and ε_∞ represents the dielectric permittivity at the high-frequency limit. According to the Equation (5), the plot of ε' and ε'' will be presented as semicircles. Generally, each semicircle represents a Debye-relaxation process. From the Cole–Cole semicircles of the residual products of the Catalyst/PE−1 system shown in Figure 5c, several semicircles are clearly observed, indicating complicated Debye-relaxation processes are existing. However, these semicircles are distorted, indicating that other forms of polarization relaxation occur in the composites, such as interfacial polarization occurs at the interfaces of air, CNTs, Fe_3C, Fe, and paraffin [34,43,49,50]. In addition, domain wall displacement, hysteresis loss, natural resonance, and eddy current loss are the causes of magnetic loss, among which, hysteresis loss mostly occurs in strong electric fields and domain wall displacement mostly occurs in the MHz frequency range, which can be excluded in this case [51–53]. Therefore, natural resonance and eddy current loss are the main contributions to magnetic loss in the sample. The eddy current loss effect can be calculated as follows:

$$C_0 = \mu''\left(\mu'\right)^{-2} f^{-1}, \tag{6}$$

According to the formula, the value of C_0 is a constant with the change of frequency when only eddy current loss acts on the dissipation of microwave energy [46,54]. As can be seen in Figure 5d, the value of C_0 is not a constant in the frequency range of 2–18 GHz, with

fluctuations between 0.0 and 0.3. Thus, the magnetic loss mechanism of the as-prepared sample is dominated by natural resonance. Moreover, the value of C_0 tends to be relatively constant in the frequency range of 14–18 GHz, confirming the presence of the eddy current loss [55].

4. Conclusions

In summary, high-yield hydrogen and high-performance MA materials were obtained from the microwave-assisted catalytic deconstruction of PE simultaneously. The concentration and yield of H_2 reached up to 67.85 vol% and 48.1 mmol $g^{-1}{}_{plastic}$, respectively, with the starting weight ratio of $FeAlO_x$ to PE at 1:1. The residual carbon exhibited remarkable MA performance with the RL_{min} value of −54.78 dB at 15 GHz and an EAB of 4.5 GHz at the thickness of 1.57 mm, which is mainly attributed to the good impedance matching, high dielectric, and magnetic loss.

Author Contributions: Formal analysis, B.Z. and P.L.; Funding acquisition, Y.Z.; Investigation, H.W. and P.L.; Methodology, Y.Z.; Project administration, Y.Z.; Supervision, K.H. and Y.Z.; Validation, H.W. and B.Z.; Writing—original draft, H.W.; Writing—review & editing, P.L. and Y.Z. All authors have read and agreed to the published version of the manuscript.

Funding: This research was funded by State Key Laboratory of Polymer Materials Engineering, grant number sklpme2021-4-04, the National Natural Science Foundation of China, grant number 61801314, and the National Natural Science Foundation of China, grant number 61731013.

Institutional Review Board Statement: Not applicable.

Informed Consent Statement: Not applicable.

Data Availability Statement: Not applicable.

Conflicts of Interest: The authors declare no conflict of interest.

References

1. Geyer, R.; Jambeck, J.R.; Law, K.L. Production, use, and fate of all plastics ever made. *Sci. Adv.* **2017**, *3*, e1700782. [CrossRef] [PubMed]
2. Thuy-Hanh, P.; Huu-Tuan, D.; Lan-Anh Phan, T.; Singh, P.; Raizada, P.; Wu, J.C.-S.; Van-Huy, N. Global challenges in microplastics: From fundamental understanding to advanced degradations toward sustainable strategies. *Chemosphere* **2021**, *267*, 129275.
3. Li, N.; Liu, H.; Cheng, Z.; Yan, B.; Chen, G.; Wang, S. Conversion of plastic waste into fuels: A critical review. *J. Hazard. Mater.* **2022**, *424*, 127460. [CrossRef] [PubMed]
4. Huang, J.; Veksha, A.; Chan, W.P.; Giannis, A.; Lisak, G. Chemical recycling of plastic waste for sustainable material management: A prospective review on catalysts and processes. *Renew. Sustain. Energy Rev.* **2022**, *154*, 111866. [CrossRef]
5. Sharma, S.S.; Batra, V.S. Production of hydrogen and carbon nanotubes via catalytic thermo-chemical conversion of plastic waste: Review. *J. Chem. Technol. Biotechnol.* **2020**, *95*, 11–19. [CrossRef]
6. Yang, R.-X.; Wu, S.-L.; Chuang, K.-H.; Wey, M.-Y. Co-production of carbon nanotubes and hydrogen from waste plastic gasification in a two-stage fluidized catalytic bed. *Renew. Energy* **2020**, *159*, 10–22. [CrossRef]
7. Yao, D.; Wu, C.; Yang, H.; Zhang, Y.; Nahil, M.A.; Chen, Y.; Williams, P.T.; Chen, H. Co-production of hydrogen and carbon nanotubes from catalytic pyrolysis of waste plastics on Ni-Fe bimetallic catalyst. *Energy Convers. Manag.* **2017**, *148*, 692–700. [CrossRef]
8. Zhang, S.; Zhu, S.; Zhang, H.; Liu, X.; Xiong, Y. High quality H-2-rich syngas production from pyrolysis-gasification of biomass and plastic wastes by Ni-Fe@Nanofibers/Porous carbon catalyst. *Int. J. Hydrogen Energy* **2019**, *44*, 26193–26203. [CrossRef]
9. Liu, X.G.; Li, B.; Geng, D.Y.; Cui, W.B.; Yang, F.; Xie, Z.G.; Kang, D.J.; Zhang, Z.D. (Fe, Ni)/C nanocapsules for electromagnetic-wave-absorber in the whole Ku-band. *Carbon* **2009**, *47*, 470–474. [CrossRef]
10. Panagopoulos, A.D.; Arapoglou, P.-D.M.; Cottis, P.G. Satellite Communications at KU, KA, and V bands: Propagation Impairments and Mitigation Techniques. *IEEE Commun. Surv. Tutor.* **2004**, *6*, 2–14. [CrossRef]
11. Chen, Z.; Xu, C.; Ma, C.; Ren, W.; Cheng, H.-M. Lightweight and Flexible Graphene Foam Composites for High-Performance Electromagnetic Interference Shielding. *Adv. Mater.* **2013**, *25*, 1296–1300. [CrossRef]
12. Huang, L.; Li, J.; Li, Y.; Heb, X.; Yuan, Y. Lightweight and flexible hybrid film based on delicate design of electrospun nanofibers for high-performance electromagnetic interference shielding. *Nanoscale* **2019**, *11*, 8616–8625. [CrossRef] [PubMed]
13. Lu, D.; Mo, Z.; Liang, B.; Yang, L.; He, Z.; Zhu, H.; Tang, Z.; Gui, X. Flexible, lightweight carbon nanotube sponges and composites for high-performance electromagnetic interference shielding. *Carbon* **2018**, *133*, 457–463. [CrossRef]

14. Liu, L.; Yang, S.; Hu, H.; Zhang, T.; Yuan, Y.; Li, Y.; He, X. Lightweight and Efficient Microwave-Absorbing Materials Based on Loofah-Sponge-Derived Hierarchically Porous Carbons. *ACS Sustain. Chem. Eng.* **2019**, *7*, 1228–1238. [CrossRef]
15. Zhao, H.; Cheng, Y.; Liu, W.; Yang, L.; Zhang, B.; Wang, L.P.; Ji, G.; Xu, Z.J. Biomass-Derived Porous Carbon-Based Nanostructures for Microwave Absorption. *Nano-Micro Lett.* **2019**, *11*, 24. [CrossRef]
16. Wu, Z.; Tian, K.; Huang, T.; Hu, W.; Xie, F.; Wang, J.; Su, M.; Li, L. Hierarchically Porous Carbons Derived from Biomasses with Excellent Microwave Absorption Performance. *ACS Appl. Mater. Interfaces* **2018**, *10*, 11108–11115. [CrossRef]
17. Zhou, C.; Geng, S.; Xu, X.; Wang, T.; Zhang, L.; Tian, X.; Yang, F.; Yang, H.; Li, Y. Lightweight hollow carbon nanospheres with tunable sizes towards enhancement in microwave absorption. *Carbon* **2016**, *108*, 234–241. [CrossRef]
18. Wang, H.; Meng, F.; Li, J.; Li, T.; Chen, Z.; Luo, H.; Zhou, Z. Carbonized Design of Hierarchical Porous Carbon/Fe_3O_4@Fe Derived from Loofah Sponge to Achieve Tunable High-Performance Microwave Absorption. *ACS Sustain. Chem. Eng.* **2018**, *6*, 11801–11810. [CrossRef]
19. Zhao, H.-B.; Cheng, J.-B.; Wang, Y.-Z. Biomass-derived Co@crystalline carbon@carbon aerogel composite with enhanced thermal stability and strong microwave absorption performance. *J. Alloys Compd.* **2018**, *736*, 71–79. [CrossRef]
20. Qiu, Y.; Yang, H.; Wen, B.; Ma, L.; Lin, Y. Facile synthesis of nickel/carbon nanotubes hybrid derived from metal organic framework as a lightweight, strong and efficient microwave absorber. *J. Colloid Interface Sci.* **2021**, *590*, 561–570. [CrossRef]
21. Jie, X.; Li, W.; Slocombe, D.; Gao, Y.; Banerjee, I.; Gonzalez-Cortes, S.; Yao, B.; AlMegren, H.; Alshihri, S.; Dilworth, J.; et al. Microwave-initiated catalytic deconstruction of plastic waste into hydrogen and high-value carbons. *Nat. Catal.* **2020**, *3*, 902–912. [CrossRef]
22. Wu, C.; Nahil, M.A.; Miskolczi, N.; Huang, J.; Williams, P.T. Processing Real-World Waste Plastics by Pyrolysis-Reforming for Hydrogen and High-Value Carbon Nanotubes. *Environ. Sci. Technol.* **2014**, *48*, 819–826. [CrossRef] [PubMed]
23. Acomb, J.C.; Wu, C.; Williams, P.T. Effect of growth temperature and feedstock:catalyst ratio on the production of carbon nanotubes and hydrogen from the pyrolysis of waste plastics. *J. Anal. Appl. Pyrolysis* **2015**, *113*, 231–238. [CrossRef]
24. Yang, R.-X.; Chuang, K.-H.; Wey, M.-Y. Effects of Nickel Species on Ni/Al_2O_3 Catalysts in Carbon Nanotube and Hydrogen Production by Waste Plastic Gasification: Bench- and Pilot-Scale Tests. *Energy Fuels* **2015**, *29*, 8178–8187. [CrossRef]
25. Fu, L.-S.; Jiang, J.-T.; Xu, C.-Y.; Zhen, L. Synthesis of hexagonal Fe microflakes with excellent microwave absorption performance. *Crystengcomm* **2012**, *14*, 6827–6832. [CrossRef]
26. Pineux, F.; Marega, R.; Stopin, A.; La Torre, A.; Garcia, Y.; Devlin, E.; Michiels, C.; Khlobystov, A.N.; Bonifazi, D. Biotechnological promises of Fe-filled CNTs for cell shepherding and magnetic fluid hyperthermia applications. *Nanoscale* **2015**, *7*, 20474–20488. [CrossRef]
27. Zhang, Y.; Liu, F. Hydrothermal conversion of graphite to carbon nanotubes (CNTs) induced by bubble collapse. *J. Phys. Chem. Solids* **2016**, *98*, 1–9. [CrossRef]
28. Brosseau, C.; Ndong, W.; Mdarhri, A. Influence of uniaxial tension on the microwave absorption properties of filled polymers. *J. Appl. Phys.* **2008**, *104*, 74907. [CrossRef]
29. Song, W.-L.; Cao, M.-S.; Hou, Z.-L.; Yuan, J.; Fang, X.-Y. High-temperature microwave absorption and evolutionary behavior of multiwalled carbon nanotube nanocomposite. *Scr. Mater.* **2009**, *61*, 201–204. [CrossRef]
30. Shao, Y.; Li, J.; Lu, W.; Xiao, J.Q.; Qiu, Y.; Chou, T.-W. Microbuckling-Enhanced Electromagnetic-Wave-Absorbing Capability of a Stretchable Fe_3O_4/Carbon Nanotube/Poly(dimethylsiloxane) Composite Film. *ACS Appl. Nano Mater.* **2018**, *1*, 2227–2236. [CrossRef]
31. Cao, M.-S.; Yang, J.; Song, W.-L.; Zhang, D.-Q.; Wen, B.; Jin, H.-B.; Hou, Z.-L.; Yuan, J. Ferroferric Oxide/Multiwalled Carbon Nanotube vs. Polyaniline/Ferroferric Oxide/Multiwalled Carbon Nanotube Multiheterostructures for Highly Effective Microwave Absorption. *ACS Appl. Mater. Interfaces* **2012**, *4*, 6949–6956. [CrossRef] [PubMed]
32. Yan, S.; Wang, L.; Wang, T.; Zhang, L.; Li, Y.; Dai, S. Synthesis and microwave absorption property of graphene oxide/carbon nanotubes modified with cauliflower-like Fe_3O_4 nanospheres. *Appl. Phys. Mater. Sci. Process.* **2016**, *122*, 235. [CrossRef]
33. Zhu, L.; Zeng, X.; Chen, M.; Yu, R. Controllable permittivity in 3D Fe_3O_4/CNTs network for remarkable microwave absorption performances. *RSC Adv.* **2017**, *7*, 26801–26808. [CrossRef]
34. Wu, G.; He, Y.; Zhan, H.; Shi, Q.Q.; Wang, J.N. A novel Fe_3O_4/carbon nanotube composite film with a cratered surface structure for effective microwave absorption. *J. Mater. Sci. Mater. Electron.* **2020**, *31*, 11508–11519. [CrossRef]
35. Li, Z.; Li, X.; Zong, Y.; Tan, G.; Sun, Y.; Lan, Y.; He, M.; Ren, Z.; Zheng, X. Solvothermal synthesis of nitrogen-doped graphene decorated by superparamagnetic Fe_3O_4 nanoparticles and their applications as enhanced synergistic microwave absorbers. *Carbon* **2017**, *115*, 493–502. [CrossRef]
36. Li, Q.; Zhu, J.; Wang, S.; Huang, F.; Liu, Q.; Kong, X. Microwave absorption on a bare biomass derived holey silica-hybridized carbon absorbent. *Carbon* **2020**, *161*, 639–646. [CrossRef]
37. Dong, S.; Hu, P.; Li, X.; Hong, C.; Zhang, X.; Han, J. $NiCo_2S_4$ nanosheets on 3D wood-derived carbon for microwave absorption. *Chem. Eng. J.* **2020**, *398*, 125588. [CrossRef]
38. Ellison, C.; McKeown, M.S.; Trabelsi, S.; Boldor, D. Dielectric Properties of Biomass/Biochar Mixtures at Microwave Frequencies. *Energies* **2017**, *10*, 502. [CrossRef]
39. Guo, L.; An, Q.-D.; Xiao, Z.-Y.; Zhai, S.-R.; Cui, L. Inherent N-Doped Honeycomb-like Carbon/Fe_3O_4 Composites with Versatility for Efficient Microwave Absorption and Wastewater Treatment. *ACS Sustain. Chem. Eng.* **2019**, *7*, 9237–9248. [CrossRef]

40. Liu, Y.; Lin, Y.; Yang, H. Facile fabrication for core-shell $BaFe_{12}O_{19}$@C composites with excellent microwave absorption properties. *J. Alloys Compd.* **2019**, *805*, 130–137. [CrossRef]
41. Yang, Q.; Yang, W.; Shi, Y.; Yu, L.; Li, X.; Yu, L.; Dong, Y.; Zhu, Y.; Fu, Y. Aligned polyaniline/porous biomass carbon composites with superior microwave absorption properties. *J. Mater. Sci. Mater. Electron.* **2019**, *30*, 1374–1382. [CrossRef]
42. Huang, L.; Li, J.; Wang, Z.; Li, Y.; He, X.; Yuan, Y. Microwave absorption enhancement of porous C@$CoFe_2O_4$ nanocomposites derived from eggshell membrane. *Carbon* **2019**, *143*, 507–516. [CrossRef]
43. Zhao, H.; Cheng, Y.; Lv, H.; Ji, G.; Du, Y. A novel hierarchically porous magnetic carbon derived from biomass for strong lightweight microwave absorption. *Carbon* **2019**, *142*, 245–253. [CrossRef]
44. Xu, Z.; He, M.; Zhou, Y.; Nie, S.; Wang, Y.; Huo, Y.; Kang, Y.; Wang, R.; Xu, R.; Peng, H.; et al. Spider web-like carbonized bacterial cellulose/$MoSe_2$ nanocomposite with enhanced microwave attenuation performance and tunable absorption bands. *Nano Res.* **2020**, *14*, 738–746. [CrossRef]
45. Zhao, B.; Shao, G.; Fan, B.; Zhao, W.; Zhang, R. Investigation of the electromagnetic absorption properties of Ni@TiO_2 and Ni@SiO_2 composite microspheres with core-shell structure. *Phys. Chem. Chem. Phys.* **2015**, *17*, 2531–2539. [CrossRef]
46. Li, N.; Huang, G.-W.; Li, Y.-Q.; Xiao, H.-M.; Feng, Q.-P.; Hu, N.; Fu, S.-Y. Enhanced Microwave Absorption Performance of Coated Carbon Nanotubes by Optimizing the Fe_3O_4 Nanocoating Structure. *ACS Appl. Mater. Interfaces* **2017**, *9*, 2973–2983. [CrossRef]
47. Huang, Q.; Bao, C.; Wang, Q.; Dong, C.; Guan, H. Tuning the microwave absorption capacity of TiP2O7 by composited with biomass carbon. *Appl. Surf. Sci.* **2020**, *515*, 145974. [CrossRef]
48. Lv, H.; Ji, G.; Liu, W.; Zhang, H.; Du, Y. Achieving hierarchical hollow carbon@Fe@Fe_3O_4 nanospheres with superior microwave absorption properties and lightweight features. *J. Mater. Chem. C* **2015**, *3*, 10232–10241. [CrossRef]
49. Wang, H.; Zhang, Y.; Wang, Q.; Jia, C.; Cai, P.; Chen, G.; Dong, C.; Guan, H. Biomass carbon derived from pine nut shells decorated with NiO nanoflakes for enhanced microwave absorption properties. *RSC Adv.* **2019**, *9*, 9126–9135. [CrossRef]
50. Guan, H.; Wang, H.; Zhang, Y.; Dong, C.; Chen, G.; Wang, Y.; Xie, J. Microwave absorption performance of $Ni(OH)_2$ decorating biomass carbon composites from Jackfruit peel. *Appl. Surf. Sci.* **2018**, *447*, 261–268. [CrossRef]
51. Liu, Z.; Zhao, N.; Shi, C.; He, F.; Liu, E.; He, C. Synthesis of three-dimensional carbon networks decorated with Fe_3O_4 nanoparticles as lightweight and broadband electromagnetic wave absorber. *J. Alloys Compd.* **2019**, *776*, 691–701. [CrossRef]
52. Du, Y.; Liu, W.; Qiang, R.; Wang, Y.; Han, X.; Ma, J.; Xu, P. Shell Thickness-Dependent Microwave Absorption of Core-Shell Fe_3O_4@C Composites. *ACS Appl. Mater. Interfaces* **2014**, *6*, 12997–13006. [CrossRef] [PubMed]
53. Dong, S.; Tang, W.; Hu, P.; Zhao, X.; Zhang, X.; Han, J.; Hu, P. Achieving Excellent Electromagnetic Wave Absorption Capabilities by Construction of MnO Nanorods on Porous Carbon Composites Derived from Natural Wood via a Simple Route. *ACS Sustain. Chem. Eng.* **2019**, *7*, 11795–11805. [CrossRef]
54. Zhu, J.; Wei, S.; Haldolaarachchige, N.; Young, D.P.; Guo, Z. Electromagnetic Field Shielding Polyurethane Nanocomposites Reinforced with Core-Shell Fe-Silica Nanoparticles. *J. Phys. Chem. C* **2011**, *115*, 15304–15310. [CrossRef]
55. Hu, P.; Dong, S.; Li, X.; Chen, J.; Hu, P. Flower-like $NiCo_2S_4$ Microspheres Based on Nanosheet Self-Assembly Anchored on 3D Biomass-Derived Carbon for Efficient Microwave Absorption. *ACS Sustain. Chem. Eng.* **2020**, *8*, 10230–10241. [CrossRef]